Acta Materialia 289 (2025) 120934

Contents lists available at ScienceDirect

Acta Materialia

journal homepage: www.elsevier.com/locate/actamat

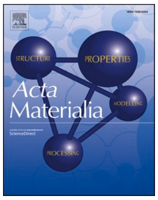

Full length article

Heterogeneous interface and vacancy engineering contribute to metastable catalysts for overall water splitting

Li Du[1], Li Bo Chen[1], Xu Liu[1], Chun Cheng Yang[*], Qing Jiang[*]

Key Laboratory of Automobile Materials (Jilin University), Ministry of Education, and School of Materials Science and Engineering, Jilin University, Changchun 130022, China

ARTICLE INFO

Keywords:
Metastable catalysts
Heterostructure
Oxygen vacancy
Water splitting
DFT calculations

ABSTRACT

Metastable catalysts usually exhibit exceptional catalytic activity, but still face the challenges of phase transition and complex synthesis, diminishing their stability and practicality. Herein, guided by density functional theory calculations, a self-supported electrode of Co, Fe-doped metastable hexagonal close-packed (hcp) Ni/NiO heterogeneous structure on nickel foam (Co, Fe-Ni/NiO/NF) was constructed by thermal shock. Spherical aberration corrected transmission electron microscopy confirms the hcp crystal structure of Ni and the phase interface of hcp Ni/NiO heterostructure. Moreover, the dynamic reaction mechanisms of the catalysts is deeply investigated by *in-situ* Raman spectroscopy. Benefitting from the co-regulation of heterogeneous interface and vacancy engineering, accompanied by the self-adjustment of active sites, this electrode exhibits superior catalytic activity and stability with low overpotentials of 26 and 215 mV for hydrogen evolution reaction and oxygen evolution reaction at 10 mA cm^{-2}. The anion exchange membrane electrolyzer comprised of the Co, Fe-Ni/NiO/NF electrodes requires only 1.48 V to drive water splitting, and achieves 1.0 A cm^{-2} at 2.55 V, showing great potential for practical applications.

1. Introduction

The development of hydrogen energy holds great significance for promoting the green energy revolution, achieving carbon neutrality goals, and fostering sustainable development [1,2]. As a green, clean, and sustainable method for hydrogen production, the electrocatalytic water splitting technology has attracted increasing attentions [3–5]. However, two pivotal half-reactions, hydrogen evolution reaction (HER) and oxygen evolution reaction (OER), in this process face the challenge of sluggish kinetics [6,7]. Although noble metal-based catalysts, such as Pt/C and IrO_2 (RuO_2), are regarded as benchmark catalysts to accelerate the reaction rates of HER and OER, respectively, the high cost significantly limits their widespread applications [8–10]. The development of high-efficiency and low-cost non-precious metal catalytic materials has emerged as a research hotspot in the field of water electrolysis [11–14].

Recently, Ni-based materials have been reported as effective catalysts in water electrolysis, which exhibit excellent performance [8, 15–18]. Among various efforts to improve their catalytic performance, heterogeneous interface construction and dual-metal doping are two prominent strategies. Firstly, the formation of heterogeneous interfaces induces electron redistribution between the two materials, thereby modulating the electronic structure of the catalyst. The synergistic effects within the heterostructure promote the conversion of reaction intermediates, improving reaction kinetics, while simultaneously stabilizing the catalyst structure to avoid aggregation or deactivation. For example, in the Ni/NiO heterostructure, the NiO surface can promote the dissociation of water and accelerate the generation of hydrogen-adsorbed species, while the Ni surface favors the adsorption and combination of these species to form H_2 [19,20]. Secondly, the dual-metal doping optimizes the adsorption strength between metals and reaction intermediates by regulating the electronic structure of the catalyst. Moreover, the synergistic effect between the metals contributes to improved structural stability, a high density of active sites, and enhanced conductivity of the catalyst [21,22]. For example, Ni and Mn dual-doping modifies the d-band center of FeP and increases electronic state density near the Fermi level, which optimizes the adsorption energy of the reaction intermediates and improves the conductivity of the catalyst [23].

Metastable catalysts with high-energy structures and unique electronic configurations usually exhibit superior catalytic activity [24,25],

---

[*] Corresponding authors.
E-mail addresses: ccyang@jlu.edu.cn (C.C. Yang), jiangq@jlu.edu.cn (Q. Jiang).

[1] These authors contributed equally to this work.

https://doi.org/10.1016/j.actamat.2025.120934
Received 7 December 2024; Received in revised form 1 March 2025; Accepted 11 March 2025

while there are two major challenges. Firstly, metastable materials are susceptible to phase transitions from high-energy to low-energy states, which may significantly diminish their original catalytic activity and stability [26,27]. Secondly, the preparation methods for metastable materials are usually intricate and rigorous, which may increase the production cost and hinder their promotion in practical applications [15,28–30]. Hence, how to enhance the stability of metastable materials and facilitate their rapid, cost-effective synthesis has become imperative.

High-temperature thermal shock, renowned for its swiftness, efficiency, broad applicability, and easy scalability, has garnered substantial attentions in the synthesis of diverse functional nanomaterials, especially in the fields of energy storage and conversion [31,32]. Such an advanced technology demonstrates its prowess in modulating the non-equilibrium thermodynamics and extreme environmental dynamics within the reaction system, and its ultra-high energy utilization efficiency, which provide strong support for the rational design, structural refinement, and large-scale fabrication of metastable micro- and nano-materials [29,33–35]. Furthermore, a myriad of defects introduced in this process, vacancies [36,37], dislocations [38,39], and grain boundaries [40], can serve as critical modulators of the electronic and energy band structure of the catalysts, thus enhancing their electrocatalytic activity and selectivity. For example, Liu et al. [38] successfully prepared dislocation-strained metastable IrNi alloy nanoparticles driven by unsteady thermal shock, which exhibited outstanding HER activity in alkaline electrolyte. Liu et al. [40] directly synthesized metastable Pd nanoparticles with abundant twin boundaries and atomic steps anchored on a carbon substrate by a solid-state thermal shock strategy for highly efficient ethanol oxidation reaction.

In this work, a self-supported electrode of Co, Fe-doped metastable hexagonal Ni/NiO heterogeneous structure on nickel foam (Co, Fe-Ni/NiO/NF) was constructed by thermal shock. This electrode boasts several compelling advantages: (1) Ni nanoparticles have a metastable hexagonal close-packed (hcp) crystal structure, which harnesses its unique electronic structure and high-energy state to facilitate the rapid electron transfer and the formation of a large number of active sites; (2) the construction of a heterogeneous interface between metastable hcp Ni and stable face-centered cubic (fcc) NiO, coupled with Co and Fe doping, not only optimizes the electronic structure of the catalyst, but also significantly enhances its stability; and (3) thermal shock can introduce defects, such as oxygen vacancies (O_V), to regulate the local coordination environment of the catalyst, thus improving its electrocatalytic activity and stability. As expected, the obtained Co, Fe-Ni/NiO/NF electrode exhibits excellent catalytic activity in alkaline media, with low overpotentials of 26 and 215 mV at 10 mA cm^{-2} for HER and OER, respectively. In addition, the anion exchange membrane (AEM) electrolyzer using this electrode as both cathode and anode requires a cell voltage of only 1.48 V to drive overall water splitting, and achieves a large current density of 1.0 A cm^{-2} at 2.55 V, accompanied by excellent stability, which underscore the enormous potential and value of this electrode system for practical applications.

2. Experimental section

2.1. Synthesis

2.1.1. Synthesis of NiCoFe LDH/NF

Before the electrodeposition, the nickel foam (NF) substrates underwent a thorough cleaning procedure with acetone and hydrochloric acid. The growth of NiCoFe LDH nanosheets on the cleaned NF substrates was initiated *via* a potentiostatic electrodeposition method. This electrochemical process employed a standard three-electrode configuration, comprising the pretreated NF as the working electrode, a graphite rod as the counter electrode, and an Ag/AgCl electrode as the reference electrode. During the electrodeposition step, a constant potential of −1.0 V vs. Ag/AgCl was applied in an electrolyte solution containing a mixture of 10.8 mM $Ni(NO_3)_2•6H_2O$, 1.2 mM $Co(NO_3)_2•6H_2O$, and 1.2 mM $FeCl_2•4H_2O$. The deposition process was maintained for 600 s. Upon completion of the electrodeposition, the as-prepared NiCoFe LDH/NF electrode was meticulously washed with water and ethanol to remove residual electrolyte, and then left to dry in a vacuum oven.

2.1.2. Synthesis of NiCoFe PBA@LDH/NF and Co, Fe-Ni/NiO/NF

The as-prepared NiCoFe LDH/NF electrode was immersed in a 30 mM $K_3[Fe(CN)_6]$ solution for 12 h to obtain the NiCoFe PBA@LDH/NF electrode. Following immersion, the electrode was thoroughly cleaned and dried. Subsequently, the NiCoFe PBA@LDH/NF electrode was directly subjected to a thermal shock treatment, wherein it was securely mounted on a copper clamp and situated within an argon-filled chamber. The thermal shock conditions were meticulously calibrated, with a voltage of 32 V, a current of 10 A, and a time-controlled shock duration of 30 s. Afterwards, the obtained sample was soaked in deionized water to eliminate superficial impurities, followed by cleaning and drying, ultimately yielding the Co, Fe-Ni/NiO/NF electrode. For a comparison, an identical thermal shock treatment was applied to the NiCoFe LDH/NF electrode, albeit without the prior immersion process in the $K_3[Fe(CN)_6]$ solution. This resulting electrode was designated as Co, Fe-NiO/NF. Besides, the Co, Fe-Ni/NiO/NF electrode was annealed at 400 °C for 4 h under Ar atmosphere. The heating rate was 2 °C min^{-1}. After cooling to room temperature, the Co, Fe-Ni(fcc)/NiO electrode was obtained.

2.2. Material characterization

The examination of morphology and microstructure features was conducted utilizing scanning electron microscopy (SEM, JSM-6700F, JEOL, 15 kV) and transmission electron microscopy (TEM, JEM-2100F, JEOL, 200 kV). To facilitate in-depth observation at the atomic scale, spherical aberration-corrected high-angle annular dark-field scanning transmission electron microscopy (HAADF-STEM, Titan Themis Z, 300 kV) was employed. X-ray diffraction (XRD) patterns were collected on a D/max2500 pc diffractometer, employing Cu Kα radiation (λ=0.15406 nm). The analysis of chemical composition and electronic state on the surface was carried out via X-ray photoelectron spectroscopy (XPS) on a Thermo ESCALAB-250Xi spectrometer, utilizing a monochromatic Al-Kα (1253.6 eV) source. *In-situ* Raman spectra were captured on a Renishaw micro-Raman spectrometer, excited by a 532 nm laser. Porosity characteristics, including specific surface area and pore size distribution, were evaluated through N_2 adsorption-desorption experiments on a Micromeritics ASAP 2020 analyzer. Inductively coupled plasma optical emission spectrometry (ICP-OES, Thermo Scientific) was used to quantify the atomic elemental ratios within the samples.

2.3. Electrochemical measurements in the half cell

The electrochemical evaluation of HER and OER performances was conducted utilizing a standard three-electrode setup integrated within an Ivium-n-Stat electrochemical workstation. The as-fabricated electrode, a graphite rod, and an Hg/HgO electrode assumed roles as the working, counter, and reference electrodes, respectively. The prepared specimens were fashioned into electrodes with a surface area of 0.5 cm^2 for assessing their electrocatalytic performance. For benchmarking, 10 mg Pt/C (20 wt%) and 10 mg RuO_2 were individually dispersed in a blend of 950 mL ethanol and 50 μL Nafion solution to formulate uniform catalyst inks, which were subsequently deposited onto the NF substrates. The polarization curves were documented at a scan rate of 5 mV s^{-1} in 1.0 M KOH electrolyte. The potential referenced to the Hg/HgO electrode was adjusted to the reversible hydrogen electrode (RHE) scale using the formula: E (vs. RHE) = E (vs. Hg/HgO) + 0.098 + 0.059 × pH. Besides, all potentials underwent *iR* compensation for accuracy. Electrochemical impedance spectroscopy (EIS) analyses were executed at initial potentials of −1.20 and 0.57 V (vs. Hg/HgO) for HER and OER, respectively, spanning frequencies from 100 kHz to 0.01 Hz with an AC amplitude of 10 mV. Additionally, the Faradic efficiencies for HER and OER were quantitatively determined *via* gas chromatography.

2.4. Electrochemical measurements in the AEM electrolyzer

The AEM electrolyzer with a 20 % Pt/C-carbon paper electrode as the cathode and an IrO_2-platinized fiber paper electrode as the anode was designated as Pt/C||IrO_2. For the electrolyzer of Co, Fe-Ni/NiO||Co, Fe-Ni/NiO, the prepared Co, Fe-Ni/NiO/NF electrode was directly employed to serve as both cathode and anode. The electrochemically active areas of these electrolyzers were precisely calibrated to 1.0 cm^2, with a specialized AEM (A80) strategically positioned to separate the cathodic and anodic compartments. The operational environment was maintained with a 1.0 M KOH electrolyte, and the temperature of the electrolysis system was controlled within a range of 25–70 °C. Linear sweep voltammetry (LSV) tests were performed on these AEM electrolyzers, spanning a voltage range from 1.2 to 3.5 V at a constant scan rate of 1 mV s^{-1}. It is pertinent to highlight that no *iR* compensation was applied to the polarization curves recorded in the LSV tests, preserving the authenticity of the voltage measurements.

3. Results and discussion

3.1. Catalyst design

To design a high-efficiency electrocatalyst towards overall water splitting, density functional theory (DFT) calculations were thoroughly conducted. The typical heterostructure models, namely Ni(fcc)/NiO, Ni (hcp)/NiO, and Co, Fe-Ni/NiO were constructed and the HER and OER catalytic mechanisms on their surfaces were further investigated. Note that Co, Fe-Ni/NiO represents the sample with Co and Fe dual-doping, metastable hcp Ni/NiO heterogeneous structures, and abundant O_V. First, the total energy of heterojunctions was examined to evaluate the potential impact of boundary conditions (**Fig. S1**). Afterwards, it is found that O_V are more easily formed at the interface than on the NiO (111) side of the heterojunction (**Fig. S2**), as the interface is inherently in a metastable state. Therefore, the sites of O_V were selected at the interface in all configurations. Next, the doping sites of Co and Fe on the heterojunction surface and their corresponding effects on the catalytic performance were investigated. To best reflect the realistic conditions, three representative positions on the heterojunction surface were randomly selected as potential doping sites (**Fig. S3**): the NiO (111) side, the Ni (002) side, and the interface. The calculations were initially carried out to determine the formation energy (ΔE_f) for Co, Fe-Ni/NiO across three representative prospective sites. The results indicate that ΔE_f is the lowest when Co and Fe doping, coupled with O_V formation, take place at Ni and NiO interface (Fig. 1**a**). Furthermore, the comparative calculations of the stability and electronic structure of the catalysts with and without Co and Fe doping were performed. The results (**Fig. S4**) reveal that the binding energy of Ni(hcp)/NiO undergoes a significant change from −1.36 eV to −4.19 eV upon Co and Fe doping at the interface, indicating a substantial enhancement in stability. Besides, the electronegativity difference between the dopants (Co and Fe) and the host atoms drives electron transfer at the interface (**Fig. S5**), which promotes the charge redistribution and consequently enhances the intrinsic activity of the catalyst. Consecutively, an investigation into the

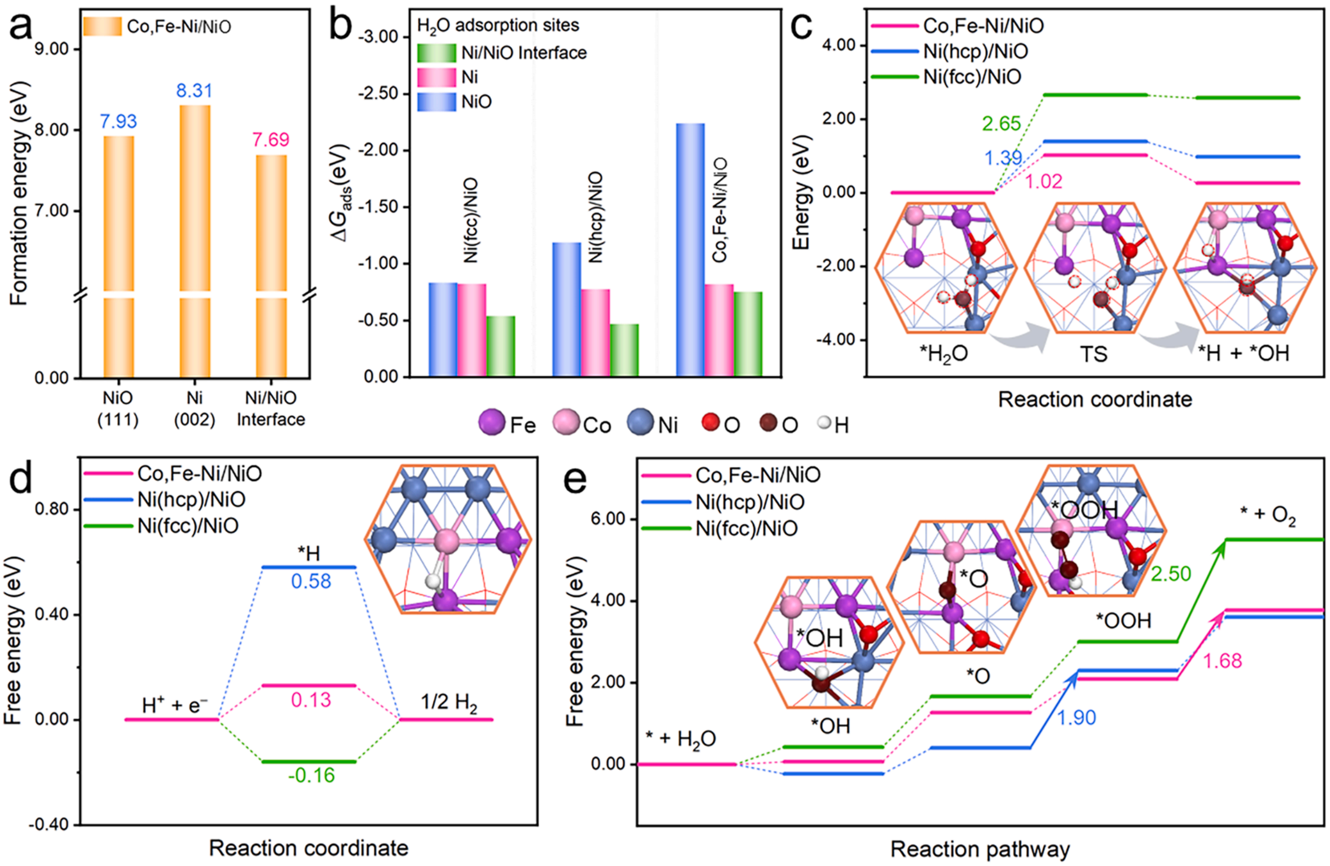

Fig. 1. DFT simulations. (a) The formation energies of Co, Fe-Ni/NiO on three prospective sites. (b) Different adsorption sites for H_2O molecules on Ni(fcc)/NiO, Ni (hcp)/NiO, and Co, Fe-Ni/NiO, respectively. All $*H_2O$ are adsorbed through Ni-O bonds. (c) Barrier calculations for the splitting of $*H_2O$ on the surfaces of these three catalysts. (d) Free energy diagrams for HER on the catalyst surfaces. The inset shows the adsorption configuration of *H on Co, Fe-Ni/NiO. (e) Free energy diagrams for OER on the catalyst surfaces. The insets show the adsorption configurations of *OH, *O, and *OOH species on Co, Fe-Ni/NiO.

optimal H_2O adsorption locations on the catalyst surface was conducted. As depicted in Fig. 1**b** and **Fig. S6**, $*H_2O$ prefer to adsorb on the Ni site of the NiO surface in each model [41]. Apparently, Ni(hcp)/NiO exhibits a much stronger ΔG_{ads} value (−1.19 eV) than that of Ni(fcc)/NiO ($\Delta G_{ads} = -0.84$ eV), indicating a better reactivity towards H_2O. Moreover, the adsorption of H_2O is significantly enhanced after introducing Co, Fe atoms and O_V into Ni(hcp)/NiO, as further confirmed by the significant interactions nearby the Fermi-energy level (E_F) and the rising d-band center in the partial density of states (PDOS) analysis (**Fig. S7**). Additionally, the kinetic energy barrier for H_2O dissociation in Fig. 1**c** also supports this finding. The energy barrier for H—OH bond cleavage in $*H_2O$ on the Co, Fe-Ni/NiO surface is estimated to be only 1.02 eV, implying that the enhanced adsorption facilitates the activation and cleavage of the H—OH bond. In contrast, the dissociation energy barriers for $*H_2O$ on Ni(fcc)/NiO and Ni(hcp)/NiO surfaces are 1.39 and 2.65 eV, respectively, rendering the dissociation of $*H_2O$ into *H energetically costlier. Hence, Co, Fe-Ni/NiO will be the primary focus of the subsequent discussions. The inset of Fig. 1c display the adsorption and dissociation processes of $*H_2O$ on the Co, Fe-Ni/NiO surface. When H_2O adsorbs onto the surface of Co, Fe-Ni/NiO, it initially occupies the Ni site in NiO. After that, the $*H_2O$ molecule is fully activated and decomposed, generating *H and *OH. Subsequently, the dissociated *H occupies the exposed Fe-Co bridge site, while *OH occupies the 3-fold hollow Fe-Ni site, and continues the subsequent protonation reaction, respectively. For HER, the strong adsorption of H hinders the desorption of the formed H_2, while weak adsorption impedes the adsorption of H^+ from the solution [42]. Consequently, a HER catalyst with $\Delta G_{*H} \approx 0$ exhibits the optimal catalytic activity [43], as it balances the adsorption and desorption of hydrogen intermediates. In terms of the catalyst design, Co, Fe-Ni/NiO is well-suited for this purpose. As shown in Fig. 1**d**, it substantially increases the adsorption of H while maintaining the facile H_2 desorption. Furthermore, for the OER mechanism, an ideal performance requires an onset potential of 1.23 V (the equilibrium potential) for the four proton-transfer steps [44]. In other words, the maximum ΔG value corresponding to the potential-determining step (PDS), should ideally approach 1.23 eV. Thus, all proton-transfer steps of these three catalysts were calculated (Fig. 1**e**). The results indicate that Co, Fe-Ni/NiO exhibits a lower PDS of 1.68 eV, compared to 1.90 eV for Ni (hcp)/NiO and 2.50 eV for Ni(fcc)/NiO. While both Co, Fe-Ni/NiO and Ni(fcc)/NiO share the *OOH to O_2 conversion as their PDS, they exhibit vastly different PDS values. This disparity can be attributed to the enhanced interfacial catalytic activity of the metastable hcp Ni [45]. Moreover, intriguingly, owing to the synergistic interactions among multiple elements, self-adjusting active sites on the Co, Fe-Ni/NiO surface are found to significantly bolster the catalytic activity. As illustrated in Fig. 1**c** and Fig. 1**e**, the calculations reveal that H_2O is initially

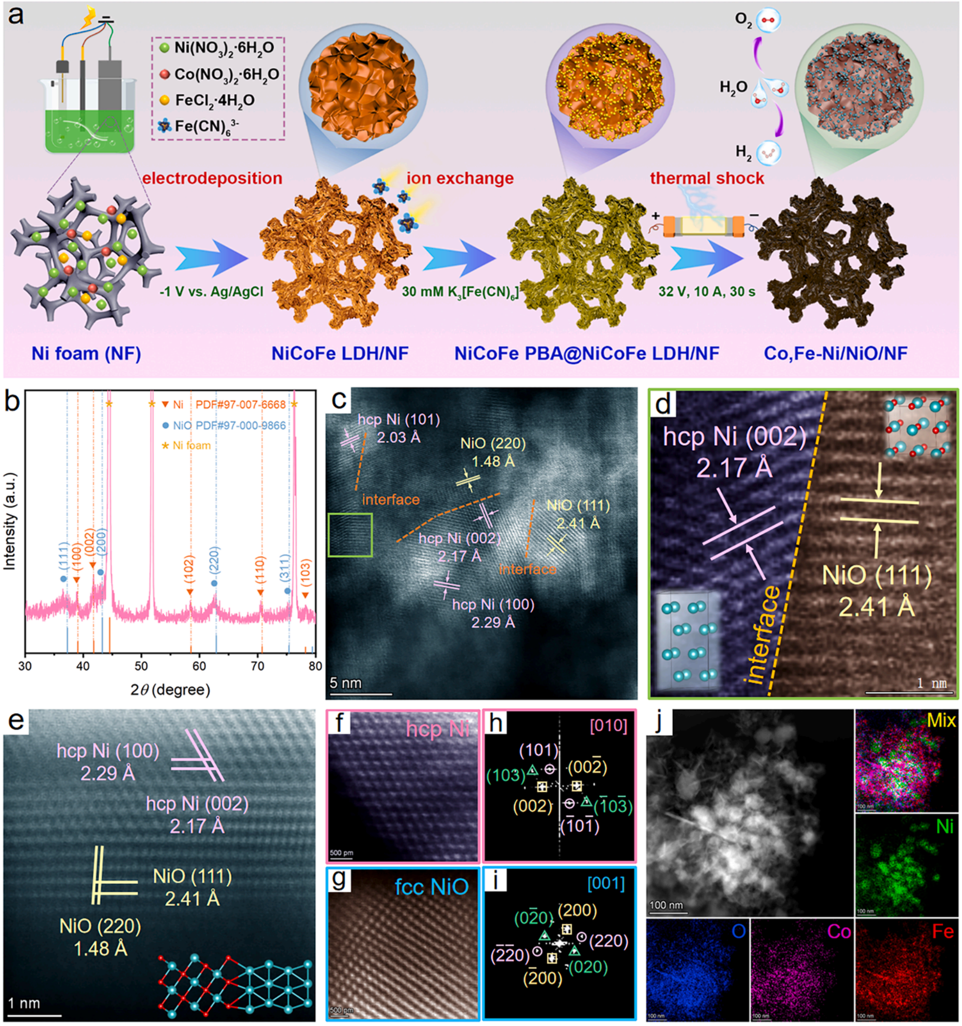

Fig. 2. Morphological and structural characterization. (a) Schematic illustration for the synthesis of Co, Fe-Ni/NiO/NF. (b) XRD pattern of Co, Fe-Ni/NiO/NF. (c) HRTEM image of Co, Fe-Ni/NiO. (d) Magnification of the green solid box in (c). (e) HAADF-STEM image of Co, Fe-Ni/NiO and the atomic arrangement of the interface between Ni and NiO is clearly shown. (f,g) HAADF-STEM images of hcp Ni and fcc NiO. (h,i) Corresponding selected-area FFT patterns of (f,g), respectively. (j) STEM image and the corresponding elements mapping (Ni, Fe, Co, O, and overlap) of Co, Fe-Ni/NiO.

adsorbed on the Ni site of the NiO (111) surface. Subsequently, the dissociated *H occupies the exposed Fe-Co bridge site, while *OH occupies the 3-fold hollow Fe-Ni site. Furthermore, the presence of O_V lowers the ΔG_{*OH} value on the Co, Fe-Ni/NiO surface compared with Ni (hcp)/NiO, facilitating the migration of oxygen-containing intermediates (*OH, *O, and *OOH) to the interface upon H_2 formation [46]. This process reduces the ΔG value of the PDS, thereby promoting the OER catalytic activity. Therefore, such a unique Co, Fe-Ni/NiO heterostructure circumvents linear scaling relationships by providing multiple active sites and optimizing the adsorption/desorption energies, which ultimately enhances the overall water splitting performance.

3.2. Material synthesis and characterization

Guided by the DFT calculations, a series of experiments were conducted. Fig. 2**a** meticulously illustrates the preparation process of Co, Fe-Ni/NiO/NF. First, NiCoFe layered double hydroxide (LDH) nanosheets were directly grown on a cleaned nickel foam substrate (NiCoFe LDH/NF, **Fig. S8** and **Fig. S9**) using electrochemical deposition. The obtained NiCoFe LDH/NF was rinsed with water and then immersed in 30 mM $K_3[Fe(CN)_6]$ solution for ion exchange, prompting the *in-situ* growth of NiCoFe Prussian blue analogue (PBA) nanoparticles on the nanosheets surface (NiCoFe PBA@LDH/NF, **Fig. S10** and **Fig. S11**). After cleaning NiCoFe PBA@LDH/NF, it was dried and subjected to a thermal shock treatment, ultimately resulting in the Co, Fe-Ni/NiO/NF sample. For a comparison, the cleaned and dried NiCoFe LDH/NF directly underwent the same thermal shock treatment, bypassing the ion exchange step. The obtained sample was denoted as Co, Fe-NiO/NF (**Fig. S12** and **Fig. S13**). The SEM images of NiCoFe LDH/NF, NiCoFe PBA@LDH/NF, and Co, Fe-NiO/NF are shown in **Fig. S14**. It can be observed that NiCoFe LDH nanosheets are uniformly grown on the Ni foam (Fig. S14a). After immersion, there are numerous nanoparticles *in-situ* grown on the nanosheets (Fig. S14b). Following the thermal shock, the nanosheet structure is maintained for Co, Fe-NiO/NF, with no significant deviation from its initial morphology (Fig. S14c).

A suite of structural and morphological characterizations were performed on Co, Fe-Ni/NiO/NF. The XRD pattern shows that the diffraction peaks at 37.2, 43.2, 62.8, and 75.3° correspond to the (111), (200), (220), and (311) planes of NiO (PDF#97–000–9866), respectively, whereas the peaks at 39.6, 41.7, 58.9, 71.9, and 78.5° correspond to the (100), (002), (102), (110), and (103) planes of hcp Ni (PDF#97–007–6668). Notably, three strong diffraction peaks at 44.6, 52.0, and 76.6° are attributed to the nickel foam substrate (Fig. 2**b**). SEM and TEM images of Co, Fe-Ni/NiO reveal a uniform distribution of nanoparticles with a diameter of approximately 18.4 nm, which are anchored on the nanosheets (**Fig. S15** and **Fig. S16**). To delve deeper into the composition and structure of the catalyst, HAADF-STEM was employed. Fig. 2**c** shows the high-resolution TEM (HRTEM) image of the sample, where the lattice spacings of 2.03, 2.17, and 2.29 Å correspond to the (101), (002), and (100) planes of hcp Ni, respectively, while the lattice spacings of 1.48 and 2.41 Å correspond to the (220) and (111) planes of NiO. By enlarging the green boxed area in Fig. 2**c**, the interface between hcp Ni and fcc NiO is discernible (Fig. 2**d**). Furthermore, the arrangement of atoms at the interface of both phases within the sample can be observed more clearly in Fig. 2**e**. The establishment of the heterojunction interface between metastable hcp Ni and stable fcc NiO, which is concurrent with a rearrangement of atomic configurations at the interface, leads to significant synergistic effects. This structural reconfiguration leads to a heightened defect concentration at the interface, and thus introduces more catalytic active sites [47,48]. Furthermore, it stimulates electron transfer and redistribution, thereby optimizing the electronic structure [16,49], and improves the electronic and ionic transport properties within the catalyst [50]. This interfacial architecture effectively mitigates the detrimental processes, such as aggregation and phase transformation of the catalyst, thereby safeguarding its activity and structural stability [27]. Sufficient evidences will be presented to illustrate the pivotal role of the heterojunction interface as below. Fig. 2**f** and Fig. 2**g** show the atomic configurations of the hcp Ni and NiO phases, and the corresponding fast Fourier transform (FFT) patterns (Fig. 2**h** and Fig. 2**i**) clearly reveal the distinct crystal planes in these two phases, respectively. Additionally, the selected area electron diffraction (SAED) pattern also shows the coexistence of hcp Ni and NiO (**Fig. S17**). Collectively, these results confirm that Ni forms a metastable hcp crystal structure and establishes a stable interface with NiO during the synthesis process. Fig. 2**j** displays the elemental constitution and distribution in Co, Fe-Ni/NiO. Note that the Ni elements exhibit a pronounced concentration in the nanoparticles, while Fe, Co, and O elements are uniformly distributed throughout the entire material. The elemental ratios in Co, Fe-Ni/NiO and its precursors were determined by ICP-OES spectroscopy, as summarized in **Table S1**. Specifically, the atomic percentages of Ni, Fe, and Co in the Co, Fe-Ni/NiO composite are 77.38 %, 15.38 %, and 7.24 %, respectively. Combining these results with prior characterizations, it can be reasonably inferred that the sample is primarily composed of Ni, with a minor fraction of Fe and Co substituting Ni lattice sites, thus incorporating into the hcp Ni phase and doping into the NiO phase. The synergistic effects of Co and Fe have been reported in the following aspects [51–54]. (1) The dual-doping of Co and Fe can optimize the electronic structure of the catalyst by jointly regulating the energy band structure and density of states, thereby optimizing the adsorption energy of the reaction intermediates and reducing the reaction energy barriers of HER and OER. (2) The dual-doping of Co and Fe can increase the number of active sites on the catalyst, which may exhibit higher catalytic activity, thereby facilitating the process of HER and OER. (3) The dual-doping of Co and Fe can also improve the stability of the catalyst. By optimizing the surface structure and electronic properties of the catalyst, deactivation and degradation during the reaction process can be reduced, thereby extending the service life of the catalyst. Specifically, Co doping generally enhances the HER performance of the catalysts by facilitating the adsorption and reduction of H^+ [51]. While the direct impact of Fe doping on HER performance may not be as pronounced as that of Co doping, it improves the catalytic activity by adjusting the electronic structure and increasing the number of active sites [52]. Moreover, Fe doping can significantly improve the OER activity by promoting the formation of higher-valence oxide species on the catalyst surface, which is favorable for the adsorption and conversion of oxygen-containing intermediates [53]. Co doping can further synergistically enhance this oxidation capability, resulting in higher OER activity [54].

Furthermore, it has been reported that the metastable hcp Ni exhibits pronounced superiority over its stable fcc Ni counterpart in catalytic performance, underpinned by two principal factors: (1) the high-energy crystal structure potentially results in abundant surface active sites, enabling more efficient adsorption and activation of reactant molecules, which is pivotal for improving the catalytic efficiency [55]; and (2) the unique electronic structure facilitates a more efficient conduit for charge mobility and transfer dynamics, thereby accelerating the overall electrocatalytic reaction and promoting superior performance [56]. Note that the term "unique electronic structure" mentioned here specifically refers to the distinct electronic configuration characteristic of metastable hcp Ni, such as the unusual distribution of electron cloud density and energy band structure compared to fcc Ni. The uniqueness mainly arises from its specific crystal structure and tight atomic arrangement [57–59]. To further substantiate this point, a comparative sample was synthesized by the annealing process of Co, Fe-Ni/NiO at 400 °C for 4 h under Ar atmosphere, which is denoted as Co, Fe-Ni(fcc)/NiO. The TEM image and corresponding SAED pattern of Co, Fe-Ni(fcc)/NiO are shown in **Fig. S18** and **Fig. S19**. Later in the discussion, a comparative analysis of the electrochemical performance between Co, Fe-Ni/NiO and Co, Fe-Ni(fcc)/NiO will be outlined.

The N_2 adsorption-desorption isotherm and the corresponding pore size distribution of Co, Fe-Ni/NiO are shown in Fig. 3**a**. This composite exhibits a high specific surface area of 101.17 m^2 g^{-1}, significantly

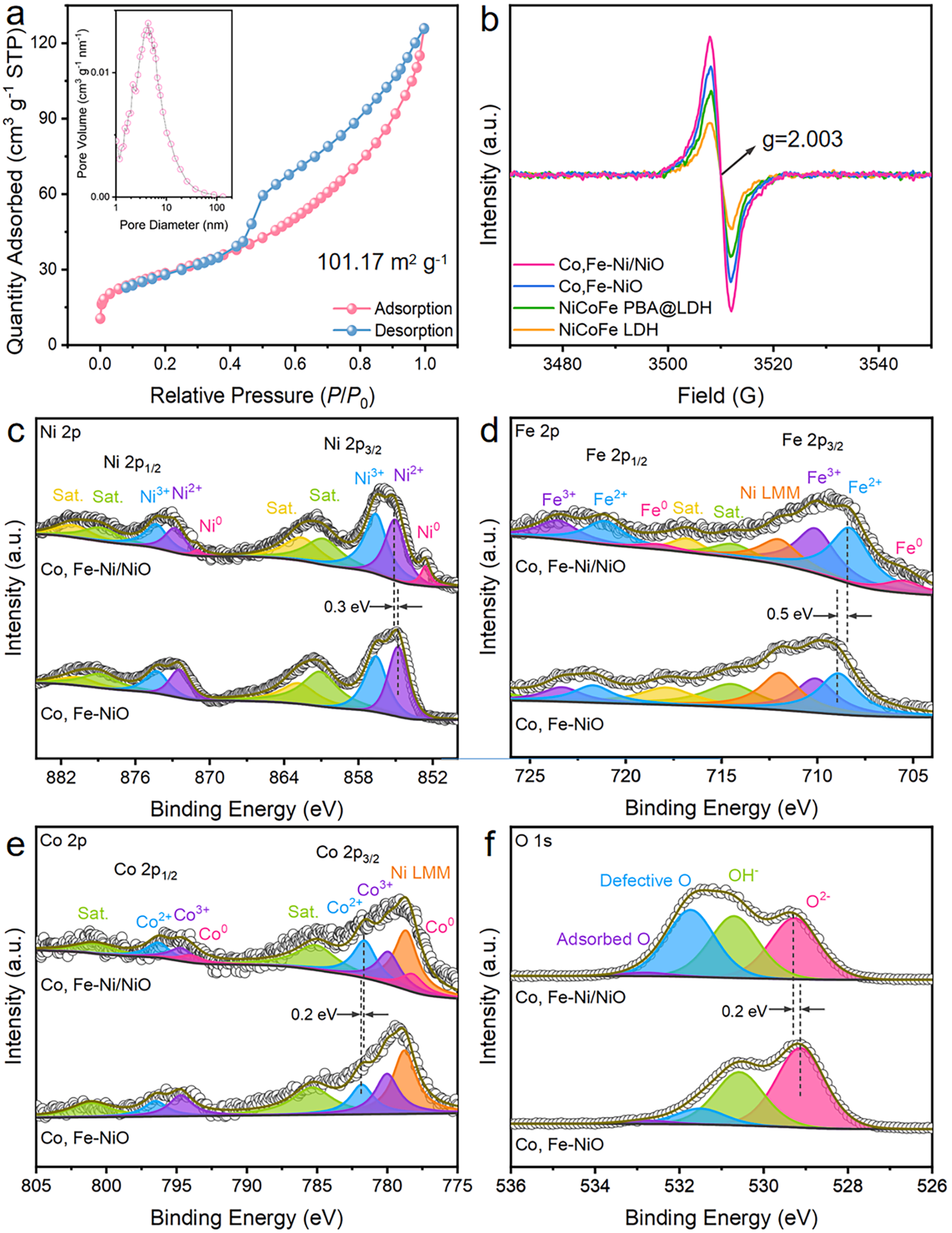

Fig. 3. Defect and electronic structure characterization. (a) N_2 adsorption/desorption isotherms and pore size distribution (the inset) of Co, Fe-Ni/NiO. (b) EPR spectra of Co, Fe-Ni/NiO, Co, Fe-NiO, and the precursors. (c-f) High-resolution XPS spectra of Ni 2p, Fe 2p, Co 2p, and O 1 s, respectively, for Co, Fe-Ni/NiO and Co, Fe-NiO.

surpassing that of NiCoFe LDH (5.83 m^2 g^{-1}, **Fig. S20**) and NiCoFe PBA@LDH (13.76 m^2 g^{-1}, **Fig. S21**), but smaller than Co, Fe-NiO (195.08 m^2 g^{-1}, **Fig. S22**). Such a phenomenon may stem from the blockage of some micropores and mesopores in the composite by nanoparticles. Intriguingly, the pore size distribution elucidates that the precursors (NiCoFe LDH and NiCoFe PBA@LDH) primarily contain a limited quantity of mesopores. The subsequent thermal shock treatment not only augments the overall pore population but also introduces micropores, culminating in a hierarchical porous structure. The micropores greatly amplify the specific surface area, thereby exposing more active sites, while the mesopores facilitate electrolyte infiltration and gas diffusion [60–62]. Fig. 3**b** shows the electron paramagnetic resonance (EPR) spectra of the samples. Compared to the precursors, the signal intensity of O_V in the thermal-shocked samples is significantly enhanced, indicating a substantial increase in the quantity of O_V. Furthermore, the higher signal intensity is observed in Co, Fe-Ni/NiO than that in Co, Fe-NiO, which may be attributed to the influence of the heterogeneous interface with elevated O_V concentration. As reported in the literature, the abundant O_V enhances the conductivity of the catalyst, regulates the adsorption of water molecule, and reduces the reaction activation energy barrier [17,63,64]. Overall, the above-mentioned hierarchical porous structure and abundant O_V in Co, Fe-Ni/NiO are attributed to the rapid cooling process inherent to the thermal shock. The elemental composition and electronic valence states on the surface of the electrodes were further investigated using XPS. The survey spectrum of Co, Fe-Ni/NiO (**Fig. S23**) reveals that the surface is composed of Ni, Fe, Co, O, and C elements. The emergence of the C signal is due to the inevitable carbon contamination stemming from air exposure. Figs. 3**c-f** display the high-resolution XPS spectra of Ni 2p, Fe 2p, Co 2p, and O 1s. Upon meticulous fitting of the results, the Ni $2p_{3/2}$ spectrum of Co, Fe-Ni/NiO reveals distinct Ni^0, Ni^{2+}, and Ni^{3+} characteristic peaks situated at 852.6, 855.1, and 856.6 eV, respectively. Similarly, the Fe $2p_{3/2}$ spectrum exhibits characteristic peaks of Fe^0, Fe^{2+}, and Fe^{3+} centered at 705.6, 708.4, and 710.2 eV, while the Co $2p_{3/2}$ spectrum comprises Co^0, Co^{3+}, and Co^{2+} characteristic peaks centered at 778.3, 780.0, and 781.7 eV. The coexistence of metallic and oxidized state characteristic peaks for Ni, Fe, and Co underscores the successful incorporation of Fe and Co into both metallic Ni and NiO matrix, reinforcing prior assumptions. In contrast, the characteristic peaks of the metallic state are absent in the spectra of Co, Fe-NiO. Notably, the Ni^{2+} peak shifts to a lower binding energy by 0.3 eV, whereas the Fe^{2+} and Co^{2+} peaks shift to higher binding energies by 0.5 and 0.2 eV, respectively. These results imply the occurrence of electron transfer and redistribution at the hcp Ni/NiO heterogeneous interface. DFT calculations have further corroborated these observations via quantitative analysis (**Fig. S5**). In the O 1s spectrum of Co, Fe-Ni/NiO, four characteristic peaks can be fitted at 529.3, 530.6, 531.6, and 532.8 eV, which are assigned to M-O bonds, M-OH bonds, defective oxygen, and adsorbed oxygen, respectively. Among them, the substantial proportion of the defective oxygen peak (**Table S2**) indicates the presence of more O_V on the surface of Co, Fe-Ni/NiO compared to Co, Fe-NiO, which is consistent with the EPR results. Unfortunately, although EPR and XPS can be utilized to detect O_V, it is difficult to determine the exact concentration and location of O_V by these two methods. Further studies should be focused on the quantitative analysis of O_V concentration and their spatial distribution.

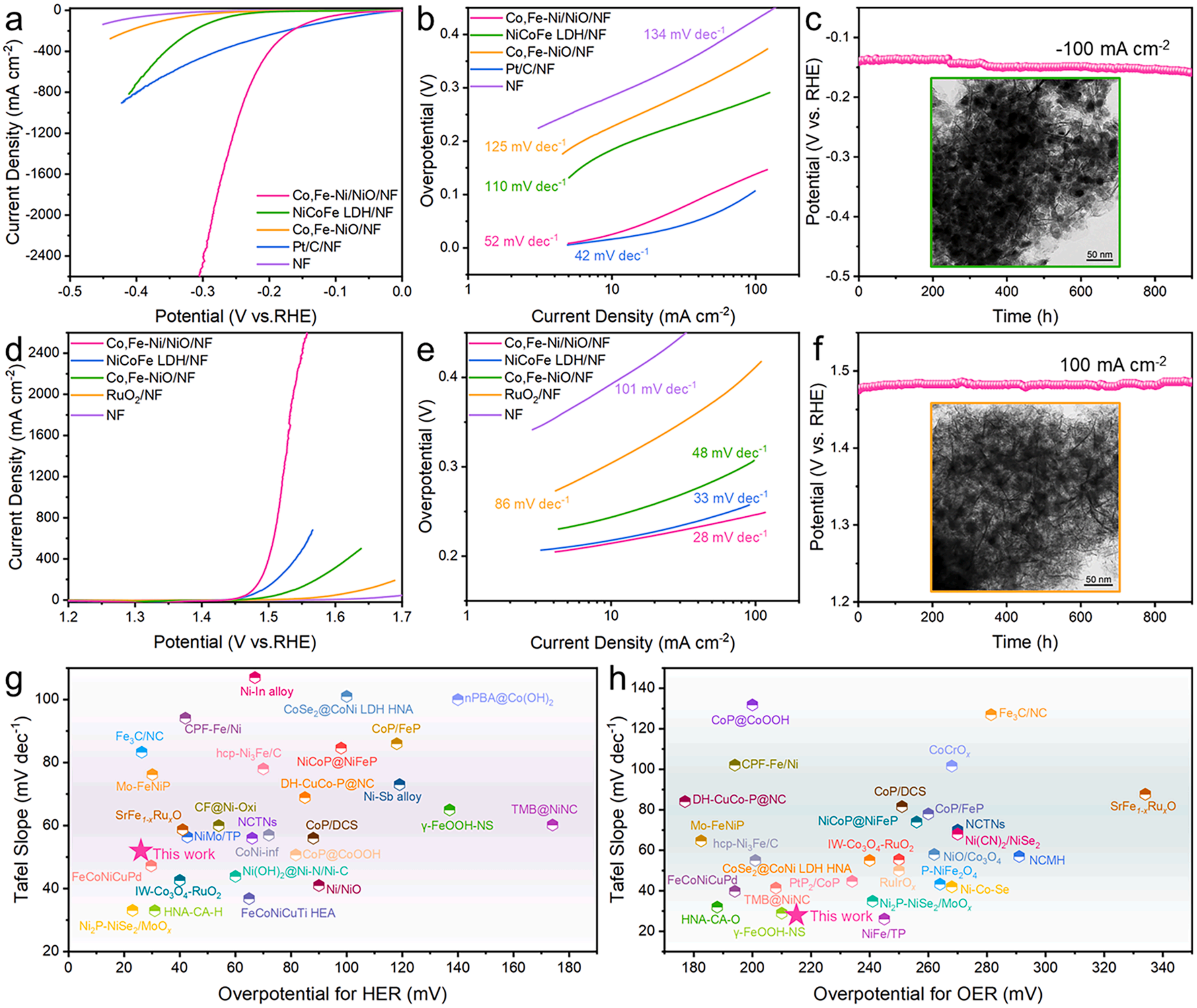

Fig. 4. HER and OER performance. (a) HER polarization curves of the Co, Fe-Ni/NiO/NF, NiCoFe LDH/NF, Co, Fe-NiO/NF, Pt/C/NF, and pure NF electrodes. (b) The corresponding HER Tafel slopes obtained from (a). (c) Chronopotentiometric curve of the Co, Fe-Ni/NiO/NF electrode at the current density of -100 mA cm^{-2}. The inset shows TEM image of Co, Fe-Ni/NiO after the HER stability test. (d) OER polarization curves of the Co, Fe-Ni/NiO/NF, NiCoFe LDH/NF, Co, Fe-NiO/NF, RuO_2/NF, and pure NF electrodes. (e) The corresponding OER Tafel slopes obtained from (d). (f) Chronopotentiometric curve of the Co, Fe-Ni/NiO/NF electrode at the current density of 100 mA cm^{-2}. The inset shows TEM image of Co, Fe-Ni/NiO after the OER stability test. (g,h) Comparisons of overpotentials at 10 mA cm^{-2} and Tafel slopes among this work and other previously reported electrocatalysts in 1.0 M KOH for HER and OER, respectively.

3.3. HER and OER performance

The electrochemical performances of the electrodes for HER and OER were evaluated in 1.0 M KOH. Firstly, the Co, Fe-Ni/NiO/NF and Co, Fe-Ni(fcc)/NiO/NF electrodes were subjected to comprehensive testing. It is evident that the Co, Fe-Ni/NiO/NF electrode demonstrates superior catalytic activity than Co, Fe-Ni(fcc)/NiO/NF for both HER and OER (**Fig. S24**), in agreement with the previously mentioned discussions. From the polarization curves in Fig. 4**a**, the Co, Fe-Ni/NiO/NF, NiCoFe LDH/NF, and Co, Fe-NiO/NF electrodes exhibit overpotentials of 26, 184, and 227 mV, respectively, to drive a current density of 10 mA cm^{-2}. Pure Ni foam also exhibits some catalytic activity for HER, but it is less active than other samples. Among them, the overpotential of the Co, Fe-Ni/NiO/NF electrode is marginally higher than that of the Pt/C/NF benchmark (17 mV). Moreover, the catalytic performance at high currents is critical for practical application, so the overpotentials at the current density of 100 mA cm^{-2} were compared. As shown in **Fig. S25**, the overpotentials of Pt/C/NF, Co, Fe-Ni/NiO/NF, NiCoFe LDH/NF, and Co, Fe-NiO/NF at 100 mA cm^{-2} are determined to be 107, 132, 281, and 360 mV, respectively, which indictes that the catalytic activity of Co, Fe-Ni/NiO/NF is almost comparable to that of Pt/C/NF. Remarkably, upon exceeding the current density of 170 mA cm^{-2}, the potential of the Co, Fe-Ni/NiO/NF electrode surpasses that of Pt/C/NF. Moreover, it achieves an impressive current density of 2.5 A cm^{-2} at a potential of −0.3 V (vs. RHE), indicating significant promise for practical applications. Turning to the kinetic insights, the corresponding Tafel slopes of Pt/C/NF, Co, Fe-Ni/NiO/NF, NiCoFe LDH/NF, Co, Fe-NiO/NF, and NF electrodes are determined to be 42, 52, 110, 125, and 134 mV dec^{-1}, respectively, as shown in Fig. 4**b**. A lower Tafel slope is indicative of a more accelerated reaction kinetics. Hence, the Co, Fe-Ni/NiO/NF electrode exhibits a low overpotential and Tafel slope, indicating its exceptional HER catalytic activity. EIS was employed to study the charge transfer properties of the electrodes (**Fig. S26**), and the corresponding equivalent circuit parameters obtained by fitting are provided in **Table S3**. By fitting to the equivalent circuit, the charge transfer resistance (R_{ct}) of Co, Fe-Ni/NiO/NF is 1.67 Ω, markedly smaller than that of Pt/C/NF (3.06 Ω), NiCoFe LDH/NF (3.76 Ω), and Co, Fe-NiO/NF (4.92 Ω). underscoring a more efficient charge transfer rate. Beyond mere catalytic activity, the assessment of the electrochemical stability is equally crucial in evaluating the overall performance of catalysts. As shown in Fig. 4**c**, upon continuous operation of the Co, Fe-Ni/NiO/NF electrode at a current density of −100 mA cm^{-2} for an extended duration of 900 h, the potential gradually decreases from an initial value of −0.134 V to −0.158 V, with a loss of only 24 mV. The inset of Fig. 4**c** presents a TEM image of the catalyst after a post-stability testing, which reveals a near-identical morphology to its pristine state. Besides, the absence of significant agglomeration or growth of nanoparticles validates the excellent long-term structural integrity and stability of the Co, Fe-Ni/NiO/NF electrode.

Subsequently, the OER performance of the electrodes was assessed by the same testing method, as depicted in Figs. 4**d-f**. The Co, Fe-Ni/NiO/NF electrode demonstrates an overpotentials of 215 mV, outperforming the NiCoFe LDH/NF (218 mV), Co, Fe-NiO/NF (244 mV), and the benchmark RuO_2/NF (304 mV) electrodes at a current density of 10 mA cm^{-2}. Besides, the overpotentials of the above electrodes at 100 mA cm^{-2} are 246, 261, 309, and 412 mV, respectively (**Fig. S25**). Among these samples, Co, Fe-Ni/NiO/NF exhibits the best OER catalytic activity, which is much better than that of RuO_2/NF. The OER catalytic activity of pure Ni foam is much lower than other samples. Additionally, the Co, Fe-Ni/NiO/NF electrode reaches a high current density of 2.5 A cm^{-2} at a modest voltage of 1.553 V (vs. RHE). The Tafel slope of Co, Fe-Ni/NiO/NF exhibits a notably low value of 28 mV dec^{-1}, compared to 33, 48, 86, and 101 mV dec^{-1} for the aforementioned other electrodes, respectively. EIS Nyquist plots (**Fig. S27**) and the specific equivalent circuit parameters obtained by fitting (**Table S4**) reveal the R_{ct} values of Co, Fe-Ni/NiO/NF (0.73 Ω), NiCoFe LDH/NF (1.04 Ω), Co, Fe-NiO/NF (2.41 Ω), and RuO_2/NF (10.17 Ω). These results convincingly indicate that the Co, Fe-Ni/NiO/NF electrode also displays excellent OER catalytic activity. To assess the long-term OER stability of the electrode, a chronopotentiometric test was conducted at a current density of 100 mA cm^{-2} with an initial potential of 1.475 V. After a continuous operation for 900 h, the potential gradually increases to 1.486 V, with an increase of merely 11 mV, affirming its outstanding OER stability. The TEM image (inset of Fig. 4**f**) shows no significant change in the morphology of the sample after the stability test, except for the presence of much finer nanosheets observed at the edge positions, which are likely the generated NiOOH species.

To gain insights into the catalytic activity of these electrodes, cyclic voltammetry (CV) tests were performed at different scan rates (**Figs. S28a, c, e** and **S29a, c**). After analysis, the double-layer capacitance (C_{dl}) value of the Co, Fe-Ni/NiO/NF electrode is determined to be 99.8 mF cm^{-2}, approximately 34 and 22 times higher than that of NiCoFe LDH/NF (2.9 mF cm^{-2}) and Co, Fe-NiO/NF (4.6 mF cm^{-2}) (**Figs. S28b, d, f**), even significantly higher than that of Pt/C/NF (48.6 mF cm^{-2}) and RuO_2/NF (24.3 mF cm^{-2}) (**Figs. S29b, d**). Because of the direct correlation between C_{dl} and the electrochemical active surface area (ECSA), these results confirm that the Co, Fe-Ni/NiO/NF electrode possesses the largest ECSA among the investigated electrodes. Consequently, the larger ECSA results in a greater number of exposed active sites, ensuring more intimate contact with the electrolyte, and thus amplifying its catalytic activity. Furthermore, from the LSV curves normalized by ECSA (**Fig. S30**), the intrinsic catalytic activity of the samples can be clearly compared. For HER, both NiCoFe LDH/NF and Co, Fe-Ni/NiO/NF exhibit high intrinsic catalytic activity, and NiCoFe LDH/NF is even better at higher current density. In terms of OER, NiCoFe LDH/NF still presents the best intrinsic catalytic activity among these samples, while Co, Fe-Ni/NiO/NF is the worst. However, both high ECSA and intrinsic catalytic activity significantly influence the performance of samples, and neither factor should be overlooked. Therefore, the excellent catalytic activity of Co, Fe-Ni/NiO/NF originates from its much higher ECSA than other two samples.

To further investigate the synergistic effects between Co and Fe, the sample without Co doping was prepared and denoted as Fe-Ni/NiO/NF. After testing, the HER and OER polarization curves of Fe-Ni/NiO/NF were obtained and compared with those of Co, Fe-Ni/NiO/NF. As shown in **Fig. S31a**, after the introduction of Co, the HER catalytic activity of Co, Fe-Ni/NiO/NF exhibits a significant improvement compared to that of Fe-Ni/NiO/NF. Besides, the Fe-Ni/NiO/NF electrode already shows relatively excellent OER activity, which is further enhanced by Co doping (see **Fig. S31b**). These experimental results corroborate the above-mentioned discussions.

Additionally, to delve into the mass transfer properties of the Co, Fe-Ni/NiO/NF electrode, multi-step chronopotentiometric tests were performed on HER (**Fig. S32**) and OER (**Fig. S33**). Faraday efficiency refers to the percentage of experimentally obtained product to its theoretical counterpart, and it is essential for augmenting the energy conversion efficiency of electrochemical reactions in practical applications. As shown in **Fig. S34** and **Fig. S35**, the Co, Fe-Ni/NiO/NF electrode achieves remarkable Faraday efficiencies of 97.8 % for both HER and OER, signifying a near-perfect congruence between the actual and theoretical gas yields. This finding suggests that the electrode operates with minimal energy loss, thus demonstrating its profound practical implication and value. A comparative analysis of the overpotentials and Tafel slopes of the Co, Fe-Ni/NiO/NF electrode with those of the catalysts reported in previous literatures (Fig. 4**g**, Fig. 4**h** and **Table S5**) reveals its superior catalytic activity for both HER and OER, outperforming the majority of non-precious metal-based catalysts.

XPS characterizations were performed on the samples after the HER and OER stability tests, denoted as post-HER and post-OER, respectively. In the post-HER sample, the characteristic peaks corresponding to the metallic and oxidized states of Ni, Fe, and Co still coexist, but the intensity of the metallic peaks decreases (**Figs. S36a-c**), indicating the occurrence of slight surface oxidation. The high-resolution spectra of Ni 2p, Fe 2p, and Co 2p for the post-OER sample (**Figs. S37a-c**) display evident changes, where the characteristic peaks in the metallic state disappear entirely, while those corresponding to Ni^{3+}, Fe^{3+}, and Co^{3+} exhibit marked enhancement. Moreover, slight shifts towards higher binding energies are observed for the characteristic peaks of Ni^{2+}, Fe^{2+}, and Co^{2+}. Additionally, the O 1 s spectrum (**Fig. S37d**) presents a significant intensification of the OH^- peak. All these results indicate the formation of oxyhydroxides on the sample surface, consistent with the *in-situ* Raman spectroscopy results. Notably, a decrease in the proportion of defective oxygen is observed in both samples (**Fig. S36d, Fig. S37d**, and **Table S2**), indicating the loss of some O_V during the long-term stability tests, which may partially account for the marginal decline in the electrode performance. Furthermore, XRD measurements were conducted to prove the stability of the metastable hcp Ni phase. In order to eliminate the potential influence of the Ni foam substrate on the diffraction peaks, the active material was scraped off the electrodes and tested in powdered form. The XRD patterns of the samples after the HER and OER stability tests are shown in **Fig. S38**. The diffraction peaks of both hcp Ni and NiO phases remain detectable, although some are less pronounced. This does not affect the determination of the sample's phase structure. Therefore, the metastable hcp Ni phase is still present in the samples after the HER and OER stability tests, demonstrating its remarkable stability throughout the reaction process. The SAED patterns of the post-HER and post-OER samples (**Fig. S39** and **Fig. S40**) reveal the persistence of diffraction rings of both hcp Ni and NiO phases, which is consistent with the XRD analysis. In particular, the metastable hcp Ni phase consistently remains stable, potentially due to the stabilizing effects induced by Fe and Co doping, along with the *in-situ* formation of a heterogeneous interface between hcp Ni and stable fcc NiO [64,65], thus enhancing the stability of the metastable phase during electrochemical reactions.

3.4. *In-situ* Raman spectroscopy

To clarify the dynamic reaction mechanisms of Co, Fe-Ni/NiO during HER and OER, *in-situ* electrochemical Raman spectroscopy tests were conducted (Fig. 5**a**). Fig. 5**b** shows the evolution of Raman spectra during OER, offering valuable insights into the structural transformations occurring at the surface of Co, Fe-Ni/NiO. Specifically, at open-circuit potential and under applied potentials below 1.4 V, the spectra exclusively exhibit a distinct peak at 535 cm^{-1}, corresponding to the Ni-O bond, alongside a broad peak at ~3400 cm^{-1}, corresponding to the interfacial water. As clearly shown in Fig. 5**c**, upon elevating the potential to 1.5 V, a pivotal transformation is observed, with the emergence of dual peaks at 475 and 555 cm^{-1}, which are assigned to γ-NiOOH and β-NiOOH phases, respectively. As the applied potential further increases, the intensity of the γ-NiOOH peak surpasses that of β-NiOOH, indicating a gradual transition from β-phase to γ-phase [66–68]. These results demonstrate the dynamic nature of the electrocatalyst surface during OER, wherein the application of higher potentials triggers a reconstruction process, leading to the oxidation of the Co, Fe-Ni/NiO surface into NiOOH species. As reported in the literature, the Ni sites in a highly oxidized state within the *in-situ* formed metal oxyhydroxide are identified as the true active centers for facilitating OER, consistently exhibiting superior catalytic activity [18,69]. Fig. 5**d** shows the Raman spectra acquired at different potentials during HER, where two prominent peaks are observed at approximately 535 and 3400

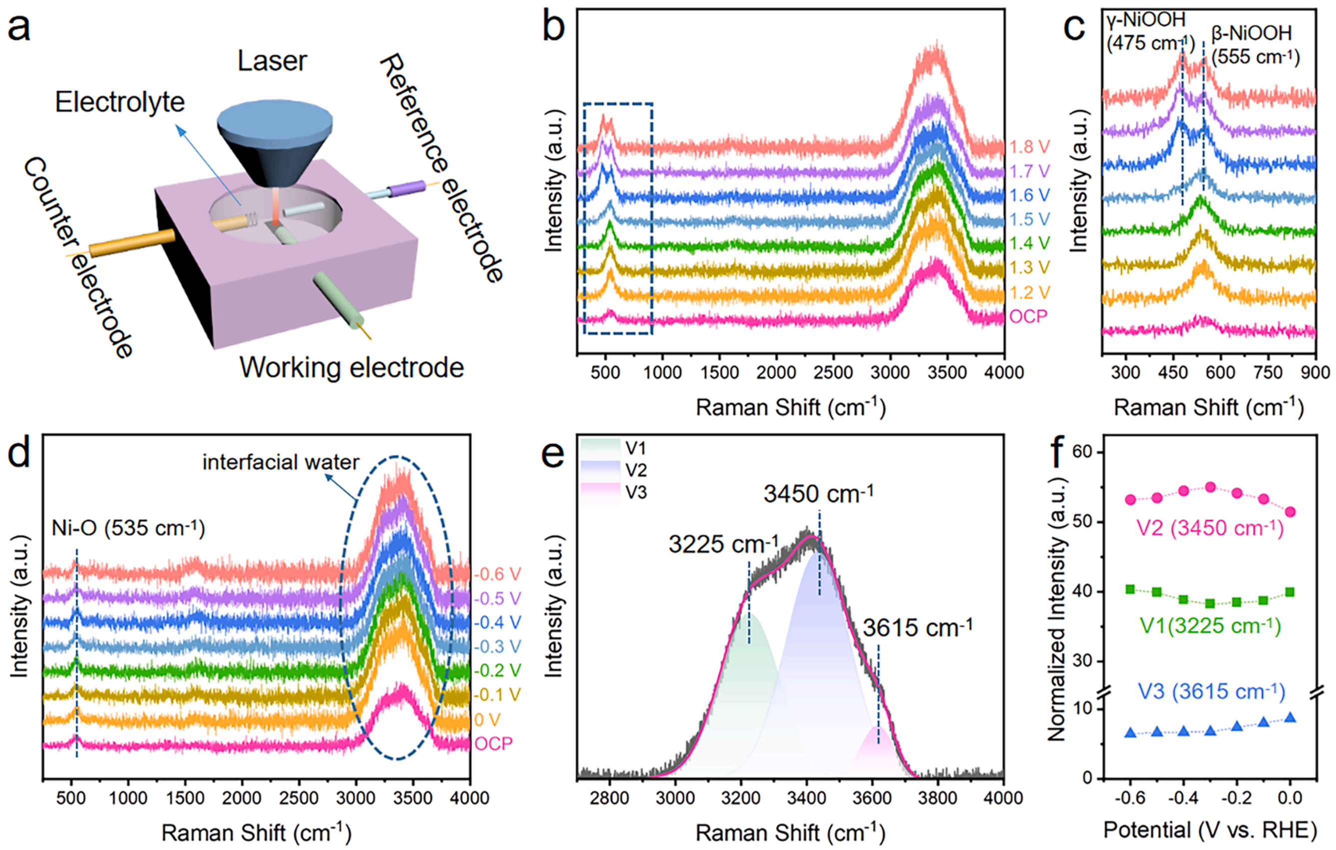

Fig. 5. *In-situ* Raman spectroscopy during HER and OER. (a) Schematic illustration of *in-situ* electrochemical Raman system. (b) *In-situ* Raman spectra of Co, Fe-Ni/NiO at open-circuit potential and under different applied potentials from 1.2 to 1.8 V during the OER process in 1.0 M KOH. (c) Enlarged view of the dashed area in (b). (d) *In-situ* Raman spectra of Co, Fe-Ni/NiO at open-circuit potential and under different applied potentials from 0 to −0.6 V during the HER process in 1.0 M KOH. (e) The three peaks of interfacial water of Co, Fe-Ni/NiO at −0.1 V. (f) Normalized intensities of the three peaks of interfacial water on Co, Fe-Ni/NiO from 0 to −0.6 V.

cm^{-1}, corresponding to the Ni-O bond and interfacial water, respectively. As the applied potential decreases from 0 to −0.6 V, the Ni-O bond peak remains relatively unchanged. Furthermore, the interfacial water peak could be meticulously deconvoluted into three peaks: V1 at 3225 cm^{-1}, V2 at 3450 cm^{-1}, and V3 at 3615 cm^{-1}, as illustrated in Fig. 5**e**. Specifically, V1 and V2 represent tetrahedrally and trigonally coordinated water molecules, respectively, at the catalyst-electrolyte interface. These species are considered as active water molecules, highly susceptible to participate in HER catalysis. Conversely, V3 corresponds to the dangling O—H bond of inactive water molecules at the interface. By fitting the interfacial water peaks at each potential and analyzing the intensity variations of these three peaks (Fig. 5**f**), a continuous decrease in the peak intensity of V3 is observed as the applied potential is lowered, which indicates the efficient dissociation of water molecules on the surface of Co, Fe-Ni/NiO [14,70]. To further bolster this argument, comparative *in-situ* Raman spectroscopy studies were performed on Co, Fe-NiO (**Fig. S41**). Specific discussions are detailed in the supporting information. These results underscore the crucial role played by the synergistic integration of abundant O_V with the excellent electronic configuration of the hcp Ni phase, which significantly accelerates the water dissociation kinetics, thereby expediting the overall HER process.

3.5. AEM water electrolyzer performance

To comprehensively evaluate the performance and practical applicability of the Co, Fe-Ni/NiO/NF electrode in industrial water electrolysis, an AEM electrolyzer (denoted as Co, Fe-Ni/NiO||Co, Fe-Ni/NiO) was assembled, directly utilizing this electrode as both cathode and anode. Fig. 6**a** illustrates the schematic representation of the AEM electrolyzer system, which fundamentally comprises an anion exchange membrane, cathode and anode electrodes, gaskets, collectors with flow channels, and end plates. Performance tests were conducted in 1.0 M KOH electrolyte at different temperatures. As a comparison, an electrolyzer assembled with Pt/C and IrO_2 as cathode and anode catalysts (Pt/C||IrO_2) was subjected to identical testing conditions. The polarization curves in Fig. 6**b** reveal that the Co, Fe-Ni/NiO||Co, Fe-Ni/NiO electrolyzer attains a current density of 10 mA cm^{-2} at a low cell voltage of 1.48 V at room temperature, significantly outperforming Pt/C||IrO_2, which requires 1.58 V. This excellent overall water splitting proficiency positions the as-prepared bi-functional catalyst among the top-performing reported in the literature (**Fig. S42**). At current densities of 0.1, 0.5, and 1.0 A cm^{-2}, the Co, Fe-Ni/NiO||Co, Fe-Ni/NiO electrolyzer exhibits cell voltages of 1.79, 2.20, and 2.55 V, respectively, whereas Pt/C||IrO_2 requires higher cell voltages to achieve the same current densities (1.86 V at 0.1 A cm^{-2}, 2.61 V at 0.5 A cm^{-2}, and 3.20 V at 1.0 A cm^{-2}). With increasing temperature, both electrolyzers exhibit enhanced performance (**Fig. S43** and **Fig. S44**). A summary of these detailed numerical values is presented in the histogram format in Fig. 6**c**, offering a clear visualization of the superior performance exhibited by the Co, Fe-Ni/NiO||Co, Fe-Ni/NiO electrolyzer. Moreover, the AEM water electrolyzer performance of this work is compared with previously reported results (**Table S6**). It is found that the performance of the Co, Fe-Ni/NiO||Co, Fe-Ni/NiO electrolyzer is comparable to some of other electrolyzers, and much better than that of the Pt/C||IrO_2 electrolyzer. Hence, it can be concluded that the Co, Fe-Ni/NiO||Co, Fe-Ni/NiO electrolyzer exhibits excellent AEM performance, but still has room for improvement. It has been reported that several factors can affect the performance of AEM electrolyzers, such as cathode/anode catalytic materials, electrolyte concentration, temperature, membrane materials, etc. The performance of our AEM electrolyzer can be optimized by adjusting these critical parameters. Further efforts will be focused on this point. Furthermore, the stability of the Co, Fe-Ni/NiO||Co, Fe-Ni/NiO electrolyzer was evaluated by chronopotentiometric

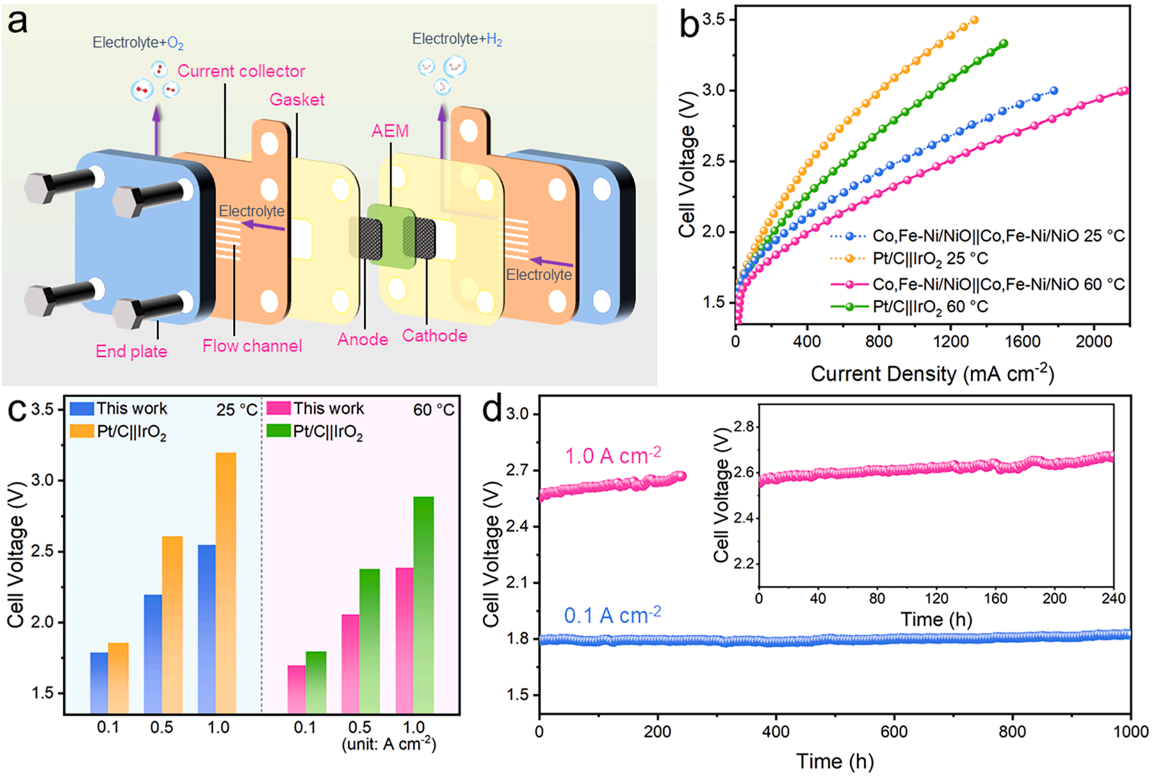

Fig. 6. AEM water electrolyzer performance. (a) Schematic illustration of the assembled AEM water electrolyzer. (b) Polarization curves of the Co, Fe-Ni/NiO||Co, Fe-Ni/NiO and Pt/C||IrO_2 electrolyzers recorded at 25 and 60 °C in 1.0 M KOH solution. (c) Comparison of the cell voltages at different current density and temperature for the Co, Fe-Ni/NiO||Co, Fe-Ni/NiO and Pt/C||IrO_2 electrolyzer. (d) Chronopotentiometric curves of the Co, Fe-Ni/NiO||Co, Fe-Ni/NiO electrolyzer at the current density of 0.1 and 1.0 A cm^{-2}, respectively.

tests. As evident in the blue *u-t* curve presented in Fig. 6**d**, the electrolyzer exhibits remarkable durability over a period of 1000 h at a current density of 0.1 A cm^{-2}, during which the cell voltage increases from 1.79 V to 1.83 V, signifying a marginal rise of 40 mV. Considering the practical relevance of higher operating currents (> 0.5 A) of the electrolyzer in real-world applications, its stability was further scrutinized at an elevated current density of 1.0 A cm^{-2} (the inset of Fig. 6**d**, depicted by the pink *u-t* curve). During the continuous water electrolysis for 240 h, the cell voltage displays a gradual but steady ascension, rising from an initial 2.55 V to 2.67 V due to the demanding operational conditions. Despite encountering a modest performance decrement of approximately 4.7 % during this process, the electrolyzer steadfastly maintains a high working efficiency, thereby highlighting its promising outlook and immense potential for practical deployment.

4. Conclusions

In summary, the adoption of thermal shock offers a viable approach for the rapid and economical fabrication of the Co, Fe-Ni/NiO/NF self-supported electrode. It displays exceptional HER and OER activity in alkaline media, with low overpotentials of 26 and 215 mV at 10 mA cm^{-2}, respectively. Moreover, the AEM electrolyzer employing these electrodes as both cathode and anode requires a cell voltage of only 1.48 V to reach 10 mA cm^{-2} at room temperature, and enables to achieve a large current density of 1.0 A cm^{-2} at 2.55 V with excellent stability. Such outstanding performance can be attributed to the heterogeneous interface between metastable hcp Ni and NiO, the abundant defects induced by thermal shock, and the dual-doping of Co and Fe. This work provides a rational design for developing high-performance catalysts and highlights their immense potential for practical applications in hydrogen production.

CRediT authorship contribution statement

Li Du: Writing – review & editing, Writing – original draft, Validation, Methodology, Investigation, Formal analysis, Data curation. **Li Bo Chen:** Writing – original draft, Validation, Methodology, Investigation, Formal analysis, Data curation. **Xu Liu:** Writing – original draft, Validation, Methodology, Investigation, Formal analysis, Data curation. **Chun Cheng Yang:** Writing – review & editing, Writing – original draft, Validation, Supervision, Resources, Project administration, Methodology, Investigation, Funding acquisition, Formal analysis, Data curation, Conceptualization. **Qing Jiang:** Writing – review & editing, Supervision, Software, Investigation, Funding acquisition, Formal analysis, Conceptualization.

Declaration of competing interest

The authors declare that they have no known competing financial interests or personal relationships that could have appeared to influence the work reported in this paper.

Acknowledgements

This project is financially supported from Science and Technology Research Project of the Education Department of Jilin Province (No. JJKH20250103BS), Science and Technology Development Program of Jilin Province (Nos. 20230402058GH, 20240101128JC), and National Natural Science Foundation of China (Nos. 52130101, U23A20546).

Supplementary materials

Supplementary material associated with this article can be found, in the online version, at doi:10.1016/j.actamat.2025.120934.

References

[1] Z. Yu, Y. Duan, X. Feng, X. Yu, M. Gao, S. Yu, Clean and affordable hydrogen fuel from alkaline water splitting: past, recent progress, and future prospects, Adv. Mater. 33 (2021) 2007100.

[2] Y. Luo, Z. Zhang, M. Chhowalla, B. Liu, Recent advances in design of electrocatalysts for high-current-density water splitting, Adv. Mater. 34 (2022) 2108133.

[3] Z.W. Seh, J. Kibsgaard, C.F. Dickens, I. Chorkendorff, J.K. Nørskov, T.F. Jaramillo, Combining theory and experiment in electrocatalysis: insights into materials design, Science 355 (2017) aad4998.

[4] P.D. Luna, C. Hahn, D. Higgins, S.A. Jaffer, T.F. Jaramillo, E.H. Sargent, What would it take for renewably powered electrosynthesis to displace petrochemical processes? Science 364 (2019) eaav3506.

[5] Y. Hou, M. Qiu, M.G. Kim, P. Liu, G. Nam, T. Zhang, X. Zhuang, B. Yang, J. Cho, M. Chen, C. Yuan, L. Lei, X. Feng, Atomically dispersed nickel–nitrogen–sulfur species anchored on porous carbon nanosheets for efficient water oxidation, Nat. Commun. 10 (2019) 1392.

[6] Y. Wang, J. Ma, J. Wang, S. Chen, H. Wang, J. Zhang, Interfacial scaffolding preparation of hierarchical PBA-based derivative electrocatalysts for efficient water splitting, Adv. Energy Mater. 9 (2019) 1802939.

[7] N.T. Suen, S.F. Hung, Q. Quan, N. Zhang, Y. Xu, H. Chen, Electrocatalysis for the oxygen evolution reaction: recent development and future perspectives, Chem. Soc. Rev. 46 (2017) 337.

[8] Q. Wang, Z. Zhang, C. Cai, M. Wang, Z. Zhao, M. Li, X. Huang, S. Han, H. Zhou, Z. Feng, L. Li, J. Li, H. Xu, J.S. Francisco, M. Gu, Single iridium atom doped Ni$_2$P catalyst for optimal oxygen evolution, J. Am. Chem. Soc. 143 (2021) 13605–13615.

[9] Q. Qin, H. Jang, L. Chen, G. Nam, X. Liu, J. Cho, Low loading of Rh$_x$P and RuP on N, P codoped carbon as two trifunctional electrocatalysts for the oxygen and hydrogen electrode reactions, Adv. Energy Mater. 8 (2018) 1801478.

[10] R. Zhang, X. Wang, S. Yu, T. Wen, X. Zhu, F. Yang, X. Sun, X. Wang, W. Hu, Ternary NiCo$_2$P$_x$ nanowires as pH-universal electrocatalysts for highly efficient hydrogen evolution reaction, Adv. Mater. 29 (2017) 1605502.

[11] D. Li, R. Xiang, F. Yu, J. Zeng, Y. Zhang, W. Zhou, L. Liao, Y. Zhang, D. Tang, H. Zhou, In situ regulating cobalt/iron oxide-oxyhydroxide exchange by dynamic iron incorporation for robust oxygen evolution at large current density, Adv. Mater. 36 (2024) 2305685.

[12] X. Yu, Y. Feng, B. Guan, X.W.(David) Lou, U. Paik, Carbon coated porous nickel phosphides nanoplates for highly efficient oxygen evolution reaction, Energy Environ. Sci. 9 (2016) 1246–1250.

[13] H. Sun, L. Chen, Y. Lian, W. Yang, L. Lin, Y. Chen, J. Xu, D. Wang, X. Yang, M. H. Rummerli, J. Guo, J. Zhong, Z. Deng, Y. Jiao, Y. Peng, S. Qiao, Topotactically transformed polygonal mesopores on ternary layered double hydroxides exposing under-coordinated metal centers for accelerated water dissociation, Adv. Mater. 32 (2020) 2006784.

[14] Q. Dai, L. Wang, K. Wang, X. Sang, Z. Li, B. Yang, J. Chen, L. Lei, L. Dai, Y. Hou, Accelerated water dissociation kinetics by electron-enriched cobalt sites for efficient alkaline hydrogen evolution, Adv. Funct. Mater. 32 (2022) 2109556.

[15] G. Wei, Y. Shen, X. Zhao, Y. Wang, W. Zhang, C. An, Hexagonal phase Ni$_3$Fe nanosheets toward high-performance water splitting by a room-temperature methane plasma method, Adv. Funct. Mater. 32 (2022) 2109709.

[16] J. Ren, L. Chen, H. Wang, W. Tian, S. Zhai, Y. Feng, Z. Yuan, Modulating interfacial charge distribution of Ni$_2$P-NiSe$_2$ by multiple interface engineering for accelerating water splitting with industry-level activity and stability, Appl. Catal. B: Environ. Energy 347 (2024) 123817.

[17] K. Wang, C. Liang, S. Li, J. Li, Z. Yi, F. Xu, Y. Wang, L. Lei, M. Zhu, S. Li, L. Zhuang, Z. Xu, Oxygen vacancy-rich nickel-iron hydroxides-derived phosphide with superaerophobic nanoarray morphology for robust overall water splitting, Sci. China Mater. 66 (2023) 2662–2671.

[18] Y. Bai, Y. Wu, X. Zhou, Y. Ye, K. Nie, J. Wang, M. Xie, Z. Zhang, Z. Liu, T. Cheng, C. Gao, Promoting nickel oxidation state transitions in single-layer NiFeB hydroxide nanosheets for efficient oxygen evolution, Nat. Commun. 13 (2022) 6094.

[19] M. Zhao, J. Wang, C. Wang, Y. Sun, P. Liu, X. Du, H. Pan, H. Li, H. Liang, J. Guo, T. Ma, Enriched edge sites of ultrathin Ni$_3$S$_2$/NiO nanomeshes promote surface reconstruction for robust electrochemical water splitting, Nano Energy 129 (2024) 110020.

[20] L. Qiao, C. Xi, C. Li, K. Zhang, Q. Li, J. Han, Y. Ding, Self-limited formation of nanoporous nickel heterostructure catalyst for electrochemical hydrogen production, Adv. Funct. Mater. 34 (2024) 2402286.

[21] L. Huang, R. Yao, X. Wang, S. Sun, X. Zhu, X. Liu, M.G. Kim, J. Lian, F. Liu, Y. Li, H. Zong, S. Han, X. Ding, *In situ* phosphating of Zn-doped bimetallic skeletons as a versatile electrocatalyst for water splitting, Energy Environ. Sci. 15 (2022) 2425.

[22] H. Li, L. Du, Y. Zhang, X. Liu, S. Li, C.C. Yang, Q. Jiang, A unique adsorption-diffusion-decomposition mechanism for hydrogen evolution reaction towards high-efficiency Cr, Fe-modified CoP nanorod catalyst, Appl. Catal. B: Environ. Energy 346 (2024) 123749.

[23] Y. Liu, Z. Zhang, L. Zhang, Y. Xia, H. Wang, H. Liu, S. Ge, J. Yu, Manipulating the d-band centers of transition metal phosphide through dual metal doping towards robust overall water splitting, J. Mater. Chem. A 10 (2022) 22125–22134.

[24] S. Chu, A. Majumdar, Opportunities and challenges for a sustainable energy future, Nature 488 (2012) 294–303.

[25] G. Sun, P. Sautet, Metastable structures in cluster catalysis from first-principles: structural ensemble in reaction conditions and metastability triggered reactivity, J. Am. Chem. Soc. 140 (2018) 2812–2820.

[26] Q. Shao, Y. Wang, S. Yang, K. Lu, Y. Zhang, C. Tang, J. Song, Y. Feng, L. Xiong, Y. Peng, Y. Li, H. Xin, X. Huang, Stabilizing and activating metastable nickel nanocrystals for highly efficient hydrogen evolution electrocatalysis, ACS Nano 12 (2018) 11625–11631.

[27] X. Tan, S. Geng, Y. Ji, Q. Shao, T. Zhu, P. Wang, Y. Li, X. Huang, Closest packing polymorphism interfaced metastable transition metal for efficient hydrogen evolution, Adv. Mater. 32 (2020) 2002857.

[28] Z. Lin, Y. Liu, U. Halim, M. Ding, Y. Liu, Y. Wang, C. Jia, P. Chen, X. Duan, C. Wang, F. Song, M. Li, C. Wan, Y. Huang, X. Duan, Solution-processable 2D semiconductors for high-performance large-area electronics, Nature 562 (2018) 254–258.

[29] X. Cui, Y. Liu, Y. Chen, Ultrafast micro/nano-manufacturing of metastable materials for energy, Natl. Sci. Rev. 11 (2024) nwae033.

[30] W. Yan, Y. Shen, C. An, L. Li, R. Si, C. An, FeO$_x$ clusters decorated hcp Ni nanosheets as inverse electrocatalyst to stimulate excellent oxygen evolution performance, Appl. Catal. B: Environ. 284 (2021) 119687.

[31] S. Dou, J. Xu, X. Cui, W. Liu, Z. Zhang, Y. Deng, W. Hu, Y. Chen, High-temperature shock enabled nanomanufacturing for energy-related applications, Adv. Energy Mater. 10 (2020) 2001331.

[32] Y. Chen, G.C. Egan, J. Wan, S. Zhu, R.J. Jacob, W. Zhou, J. Dai, Y. Wang, V. A. Danner, Y. Yao, K. Fu, Y. Wang, W. Bao, T. Li, M.R. Zachariah, L. Hu, Ultra-fast self-assembly and stabilization of reactive nanoparticles in reduced graphene oxide films, Nat. Commun. 7 (2016) 12332.

[33] Y. Yao, Z. Huang, P. Xie, S.D. Lacey, R.J. Jacob, H. Xie, F. Chen, A. Nie, T. Pu, M. Rehwoldt, D. Yu, M.R. Zachariah, C. Wang, R. Shahbazian-Yassar, J. Li, L. Hu, Carbothermal shock synthesis of high-entropy-alloy nanoparticles, Science 359 (2018) 1489–1494.

[34] Y. Yao, Z. Huang, P. Xie, L. Wu, L. Ma, T. Li, Z. Pang, M. Jiao, Z. Liang, J. Gao, Y. He, D.J. Kline, M.R. Zachariah, C. Wang, J. Lu, T. Wu, T. Li, C. Wang, R. Shahbazian-Yassar, L. Hu, High temperature shockwave stabilized single atoms, Nat. Nanotechnol. 14 (2019) 851–857.

[35] K.M. Wyss, D.X. Luong, J.M. Tour, Large-scale syntheses of 2D materials: flash joule heating and other methods, Adv. Mater. 34 (2022) 2106970.

[36] C. Liu, W. Zhou, J. Zhang, Z. Chen, S. Liu, Y. Zhang, J. Yang, L. Xu, W. Hu, Y. Chen, Y. Deng, Air-assisted transient synthesis of metastable nickel oxide boosting alkaline fuel oxidation reaction, Adv. Energy Mater. 10 (2020) 2001397.

[37] W. Chen, Z. Wang, K.V. Bets, D.X. Luong, M. Ren, M.G. Stanford, E.A. McHugh, W. A. Algozeeb, H. Guo, G. Gao, B. Deng, J. Chen, J. Li, W.T. Carsten, B.I. Yakobson, J. M. Tour, Millisecond conversion of metasTable 2D materials by flash joule heating, ACS Nano 15 (2021) 1282–1290.

[38] S. Liu, Z. Hu, Y. Wu, J. Zhang, Y. Zhang, B. Cui, C. Liu, S. Hu, N. Zhao, X. Han, A. Cao, Y. Chen, Y. Deng, W. Hu, Dislocation-strained IrNi alloy nanoparticles driven by thermal shock for the hydrogen evolution reaction, Adv. Mater. 32 (2020) 2006034.

[39] S. Liu, Y. Shen, Y. Zhang, B. Cui, S. Xi, J. Zhang, L. Xu, S. Zhu, Y. Chen, Y. Deng, W. Hu, Extreme environmental thermal shock induced dislocation-rich Pt nanoparticles boosting hydrogen evolution reaction, Adv. Mater. 34 (2022) 2106973.

[40] C. Liu, Y. Shen, J. Zhang, G. Li, X. Zheng, X. Han, L. Xu, S. Zhu, Y. Chen, Y. Deng, W. Hu, Multiple twin boundary-regulated metastable Pd for ethanol oxidation reaction, Adv. Energy Mater. 12 (2022) 2103505.

[41] L. Zhao, Y. Zhang, Z. Zhao, Q. Zhang, L. Huang, L. Gu, G. Lu, J. Hu, L. Wan, Steering elementary steps towards efficient alkaline hydrogen evolution via size-dependent Ni/NiO nanoscale heterosurfaces, Natl. Sci. Rev. 7 (2020) 27–36.

[42] J. Zhang, H. Zhou, Y. Liu, J. Zhang, Y. Cui, J. Li, J. Lian, G. Wang, Q. Jiang, Interface engineering of CoP$_3$/Ni$_2$P for boosting the wide pH range water-splitting activity, ACS Appl. Mater. Interfaces 13 (2021) 52598–52609.

[43] L. Chen, Z. Chen, Y. Wang, C. Yang, Q. Jiang, Design of dual-modified MoS$_2$ with nanoporous Ni and graphene as efficient catalysts for the hydrogen evolution reaction, ACS Catal 8 (2018) 8107–8114.

[44] D. Wang, Z. Chen, K. Gu, C. Chen, Y. Liu, X. Wei, C.V. Singh, S. Wang, Hexagonal cobalt nanosheets for high-performance electrocatalytic NO reduction to NH$_3$, J. Am. Chem. Soc. 145 (2023) 6899–6904.

[45] Z. Li, X. Wen, F. Chen, Q. Zhang, Q. Zhang, L. Gu, J. Cheng, B. Wu, N. Zheng, Hexagonal nickel as a highly durable and active catalyst for hydrogen evolution, ACS Catal 11 (2021) 8798–8806.

[46] Y.R. Pei, H.Y. Zhou, M. Zhao, J.C. Li, X. Ge, W. Zhang, C.C. Yang, Q. Jiang, High-efficiency sodium storage of Co$_{0.85}$Se/WSe$_2$ encapsulated in N-doped carbon polyhedron via vacancy and heterojunction engineering, Carbon Energy 6 (2024) e374.

[47] Z. An, H. Xue, J. Sun, N. Guo, T. Song, J. Sun, Y. Hao, Q. Wang, Co-construction of sulfur vacancies and heterogeneous interface into Ni$_3$S$_2$/MoS$_2$ catalysts to achieve highly efficient overall water splitting, Chin. J. Struct. Chem. 41 (2022) 2208037–2208043.

[48] J. Zhang, J. Qian, J. Ran, P. Xi, L. Yang, D. Gao, Engineering lower coordination atoms onto NiO/Co$_3$O$_4$ heterointerfaces for boosting oxygen evolution reactions, ACS Catal 10 (2020) 12376–12384.

[49] P. Zhai, C. Wang, Y. Zhao, Y. Zhang, J. Gao, L. Sun, J. Hou, Regulating electronic states of nitride/hydroxide to accelerate kinetics for oxygen evolution at large current density, Nat. Commun. 14 (2023) 1873.

[50] X. Zheng, X. Han, Y. Cao, Y. Zhang, D. Nordlund, J. Wang, S. Chou, H. Liu, L. Li, C. Zhong, Y. Deng, W. Hu, Identifying dense NiSe$_2$/CoSe$_2$ heterointerfaces coupled with surface high-valence bimetallic sites for synergistically enhanced oxygen electrocatalysis, Adv. Mater. 32 (2020) 2000607.

[51] X. Song, C. Fan, Y. Tang, Y. Ren, Z. Zang, L. Li, X. Yu, Z. Lu, X. Yang, X. Zhang, The effects of Co doping for Fe metal on boosting hydrogen and oxygen evolution reactions, Fuel 381 (2025) 133558.

[52] J. Wang, S. Xin, Y. Xiao, Z. Zhang, Z. Li, W. Zhang, C. Li, R. Bao, J. Peng, J. Yi, S. Chou, Manipulating the water dissociation electrocatalytic sites of bimetallic nickel-based alloys for highly efficient alkaline hydrogen evolution, Angew. Chem. Int. Ed. 61 (2022) e202202518.

[53] H. Lv, Y. Gao, D.S. Li, A. Yu, C. Sun, C. Zhang, Mediation of oxidation and spin states of Fe/P-CoO$_2$ core-shell structures catalysts for oxygen evolution reaction, Adv. Funct. Mater. (2024) 2418334.

[54] H.J. Niu, N. Ran, W. Zhou, W. An, C. Huang, W. Chen, M. Zhou, W.F. Lin, J. Liu, L. Guo, Synergistic atomic environment optimization of nickel-iron dual sites by Co doping and Cr vacancy for electrocatalytic oxygen evolution, J. Am. Chem. Soc. 147 (2025) 2607–2615.

[55] K. Liu, H. Yang, Y. Jiang, Z. Liu, S. Zhang, Z. Zhang, Z. Qiao, Y. Lu, T. Cheng, O. Terasaki, Q. Zhang, C. Gao, Coherent hexagonal platinum skin on nickel nanocrystals for enhanced hydrogen evolution activity, Nat. Commun. 14 (2023) 2424.

[56] S. Geng, Y. Ji, J. Su, Z. Hu, M. Fang, D. Wang, S. Liu, L. Li, Y. Li, J. Chen, J.F. Lee, X. Huang, Q. Shao, Homogeneous metastable hexagonal phase iridium enhances hydrogen evolution catalysis, Adv. Sci. 10 (2023) 2206063.

[57] H.R. Pan, Z.Q. Shi, X.Z. Liu, S. Jin, J. Fu, L. Ding, S.Q. Wang, J. Li, L. Zhang, D. Su, C. Ling, Y. Huang, C. Xu, T. Tang, J.S. Hu, Unconventional *hcp/fcc* nickel heteronanocrystal with asymmetric convex sites boosts hydrogen oxidation, Angew. Chem. Int. Ed. 63 (2024) e202409763.

[58] J. Zhuang, X. Liu, Y. Ji, F. Gu, J. Xu, Y. Han, G. Xu, Z. Zhong, F. Su, Phase-controlled synthesis of Ni nanocrystals with high catalytic activity in 4-nitrophenol reduction, J. Mater. Chem. A 8 (2020) 22143–22154.

[59] J. Zhuang, F. He, X. Liu, P. Si, F. Gu, J. Xu, Y. Wang, G. Xu, Z. Zhong, F. Su, *In-situ* growth of heterophase Ni nanocrystals on graphene for enhanced catalytic reduction of 4-nitrophenol, Nano Res 15 (2022) 1230–1237.

[60] Y. Gao, D. Zheng, Q. Li, W. Xiao, T. Ma, Y. Fu, Z. Wu, L. Wang, 3D Co$_3$O$_4$-RuO$_2$ hollow spheres with abundant interfaces as advanced trifunctional electrocatalyst for water-splitting and flexible Zn–air battery, Adv. Funct. Mater. 32 (2022) 2203206.

[61] C.C. Yang, S.F. Zai, Y.T. Zhou, L. Du, Q. Jiang, Fe$_3$C-Co nanoparticles encapsulated in a hierarchical structure of N-doped carbon as a multifunctional electrocatalyst for ORR, OER, and HER, Adv. Funct. Mater. 29 (2019) 1901949.

[62] W. Xi, G. Yan, Z. Lang, Y. Ma, H. Tan, H. Zhu, Y. Wang, Y. Li, Oxygen-doped nickel iron phosphide nanocube arrays grown on Ni foam for oxygen evolution electrocatalysis, Small 14 (2018) 1802204.

[63] L. Du, X. Gao, G. Wang, C. Yang, Q. Jiang, CeO$_2$ nanoparticles decorated on porous Ni-Fe bimetallic phosphide nanosheets for high-efficient overall water splitting, Mater. Res. Lett. 11 (2023) 159–167.

[64] Y. Chen, Y. Liu, W. Zhai, H. Liu, T. Sakthivel, S. Guo, Z. Dai, Metastabilizing the ruthenium clusters by interfacial oxygen vacancies for boosted water splitting electrocatalysis, Adv. Energy Mater. 14 (2024) 2400059.

[65] I.A. Cechanaviciute, R.P. Antony, O.A. Krysiak, T. Quast, S. Dieckhöfer, S. Saddeler, P. Telaar, Y.T. Chen, M. Muhler, W. Schuhmann, Scalable synthesis of multi-metal electrocatalyst powders and electrodes and their application for oxygen evolution and water splitting, Angew. Chem. Int. Ed. 62 (2023) e202218493.

[66] R.N. Dürr, P. Maltoni, H. Tian, B. Jousselme, L. Hammarström, T. Edvinsson, From NiMoO$_4$ to γ NiOOH: detecting the active catalyst phase by time resolved *in situ* and operando raman spectroscopy, ACS Nano 15 (2021) 13504–13515.

[67] Z. Qiu, Y. Ma, T. Edvinsson, In operando Raman investigation of Fe doping influence on catalytic NiO intermediates for enhanced overall water splitting, Nano Energy 66 (2019) 104118.

[68] L. Wu, M. Ning, X. Xing, Y. Wang, F. Zhang, G. Gao, S. Song, D. Wang, C. Yuan, L. Yu, J. Bao, S. Chen, Z. Ren, Boosting oxygen evolution reaction of (Fe, Ni)OOH via defect engineering for anion exchange membrane water electrolysis under industrial conditions, Adv. Mater. 35 (2023) 2306097.

[69] Y. Zhu, M. Klingenhof, C. Gao, T. Koketsu, G. Weiser, Y. Pi, S. Liu, L. Sui, J. Hou, J. Li, H. Jiang, L. Xu, W. Huang, C. Pao, M. Yang, Z. Hu, P. Strasser, J. Ma, Facilitating alkaline hydrogen evolution reaction on the hetero-interfaced Ru/RuO$_2$ through Pt single atoms doping, Nat. Commun. 15 (2024) 1447.

[70] X. Mu, X. Zhang, Z. Chen, Y. Gao, M. Yu, D. Chen, H. Pan, S. Liu, D. Wang, S. Mu, Constructing symmetry-mismatched Ru$_x$Fe$_{3-x}$O$_4$ heterointerface-supported Ru clusters for efficient hydrogen evolution and oxidation reactions, Nano Lett 24 (2024) 1015–1023.